

# Experimental Investigation of Electro spraying Properties Based on Ring Electrode Modification

Ji Yeop Kim, Sang Ji Lee, Mun Hee Lee, and Jung Goo Hong\*



Cite This: *ACS Omega* 2024, 9, 1125–1133



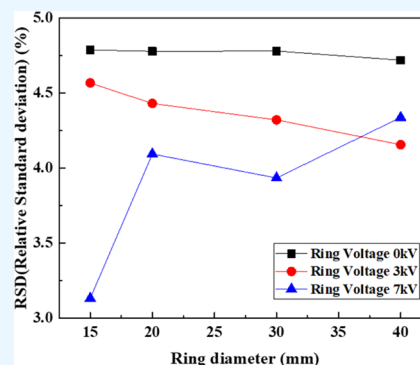
Read Online

ACCESS |

Metrics & More

Article Recommendations

**ABSTRACT:** Electro spraying uses a high-voltage potential difference to create fine droplets. This study conducts a comparative analysis of the spray pattern and droplet properties using ring electrode parameters. The spray pattern and droplet characteristics are analyzed based on the experimental parameters of the ring electrode. The results show that the cone-jet mode forms quickly for the ring electrode. In addition, as the ring diameter decreases, the ring voltage increases and an increase in the distance between the ring and the nozzle in the bottom direction decreases the Sauter mean diameter and its standard deviation. The optimal conditions for the formation of fine and uniform droplets include a ring diameter of 15 mm, a ring voltage of 7 kV, and a nozzle-to-ring distance of (+) 20 mm.



## 1. INTRODUCTION

Food drying is a method used to remove moisture normally contained in food. This is beneficial for storage and transportation and provides food in a nonperishable state.<sup>1–3</sup> Common methods of food drying include hot-air drying,<sup>4</sup> freeze-drying,<sup>5</sup> and spray drying.<sup>6</sup>

Among them, spray drying is widely used to coat food product activators with heat- and acid-sensitive coating; however, the product must be spray-dried with the most optimized material to achieve its desired properties.<sup>6</sup> And spray drying is the most commonly used conventional method for the production of foods, pharmaceuticals, and compounds owing to its short drying time and simplicity compared to other drying methods, offering low energy consumption compared to conventional methods and enabling scale-up and simplification.<sup>7,8</sup>

Hot air, freezing, and power failure, among others, are used when spray drying is performed to solidify liquid. Rotary disks and hydraulics are employed for hot air, and a large surface area is utilized for solvent evaporation by atomizing the liquid in heated gas.<sup>9</sup> This allows for quick drying and is less expensive. However, spray drying requires high heat, consuming high energy, and creating a hospitable environment for microorganisms (e.g., bacteria). In addition, most liquids are delivered by a pump, which can cause clogging in the case of highly viscous liquids.<sup>9,10</sup> In freezing, frozen droplets are dried in a lyophilizer by spraying them with a cryogenic liquid such as liquid nitrogen. The dried droplet size is easier to control than that in conventional hot-air drying and can preserve microorganisms that cannot tolerate high temper-

atures. However, it requires high energy, has a long turnaround time, and is 30–50 times more expensive than hot-air drying.<sup>10</sup> The drying of high-molecular-weight materials is critical for efficient food production.<sup>11</sup> Traditional hot-air methods are limited to viscous materials, whereas freezing requires long processing times and high costs. Therefore, capacitive spray drying is considered to address the shortcomings of both methods.<sup>12,13</sup> Capacitive spray dryers can compensate for the rotary disks' inability to take advantage of the high viscosity.<sup>13</sup> They can micronize many high-molecular-weight solutions and exhibit high efficiency.<sup>14,15</sup> Unlike a dielectric nozzle, the fluid surface is charged during atomization; hence, uniform droplets are formed as they do not polymerize and coalesce under the force of gravity.<sup>16</sup> In addition, droplets atomized via capacitive spray drying have minimal surface exposure of the active ingredient and rapid dissolution capabilities, which are favorable for encapsulation and can be stored for long periods, making them applicable to shelf life-sensitive products, such as drugs, probiotics, and proteins.<sup>17–21</sup> Electrostatic atomization provides excellent flowability owing to the generation of uniform droplets.<sup>22</sup> It offers simplicity with no postprocessing systems such as cyclones and bag filters. Lastly, it exhibits environmental friendliness because no downstream droplet

**Received:** September 25, 2023

**Revised:** December 13, 2023

**Accepted:** December 21, 2023

**Published:** December 28, 2023



processing is necessary.<sup>23</sup> The system can be operated at lower temperatures (80 °C) compared to spray dryers (150–200 °C), reducing energy consumption compared to other conventional systems.<sup>24</sup>

In food drying, these electro spraying properties enable rapid drying at lower temperatures, prevent nutrient destruction, delay oxidation, and retain color and highly volatile acetaldehyde.<sup>25,26</sup>

Various spraying modes have been developed based on experimental conditions and fluidic properties.<sup>27</sup> The most commonly used spraying mode is the cone-jet mode. Its conical shape is formed when the electric field (voltage) and surface tension are parallel to each other. In particular, the charge coming out of the nozzle tip forms an equal charge distribution. The cone is formed, provided that sufficient relaxation time is set.<sup>28</sup> In the cone-jet mode, the fluid pattern blasted from the nozzle tip produces a triangular pyramid shape. The tip shear tension causes the tip to break into droplets because of an external disturbance.<sup>29</sup> According to Taylor,<sup>28</sup> the theoretical half-angle of the cone is 49.3°, resulting in a consistent and continuous spray pattern.<sup>30</sup>

Compared to other electro spraying modes, cone-jet spraying is more stable, can continuously produce more homogeneous droplets, and has a higher water concentration. The droplet characteristic can easily be changed by modifying the external environment.<sup>31</sup> In addition, the cone-jet mode possesses excellent spray pattern repeatability;<sup>32</sup> thus, it is used in a wide range of applications, including local-area cooling, mass spectrometry, nanofilm production, nanometal wire production, and semiconductor processing.<sup>33,34</sup>

However, this mode can only be tested under an applied voltage with a limited scope owing to the complexity of both experimental and fluidic properties.<sup>35</sup> Consequently, expressing the spraying mode by applying a voltage as a dimensionless number becomes difficult. The applied voltage must be evaluated, and its characteristics must be determined depending on various conditions (experimental parameters).

In the ring electrode system, a ring electrode is attached to the existing nozzle and substrate while a high voltage is being applied.<sup>36</sup> The ring electrode system can readily change the spray pattern by altering the external conditions, thereby adjusting the droplet size, speed, and distribution. This system is used for local film coatings with high water concentrations and areas, such as microburners, where fluidic characteristics and experimental parameters are established. Therefore, the droplet size, speed, and distribution must be controlled.<sup>37,38</sup>

Ali<sup>39</sup> reported that the applied voltage required for cone-jet generation increases with the flow rate, contradicting the results of Liao,<sup>40</sup> who concluded that the cone jet is independent of the flow rate. According to Kim,<sup>41</sup> the cone-jet mode might be delayed depending on the distance between the nozzle and the substrate. Tang and Kebarle<sup>42</sup> confirmed that the applied voltage in the cone-jet mode is delayed based on the nozzle diameter. Regarding the droplet size and distribution, Tang<sup>43</sup> showed that the droplet size decreases with the distance between the nozzle and the substrate. Le<sup>44</sup> investigated the droplet size and distribution under various spraying modes and flow conditions. In the case of the ring electrode system, Kuwahata<sup>38</sup> evaluated the electric field generated based on the ring electrode, whereas Gan<sup>45</sup> verified that a high speed can be observed in the presence of a ring electrode. The ring electrode enhanced the droplet distribution compared to that achieved without droplet dispersion.

The aforementioned experiments and analyses have overlooked the effects of the location, structure, and applied voltage of the ring electrode. Information about the applied voltage and spray properties related to the presence and absence of ring electrodes is lacking. Therefore, spray characteristics must be evaluated based on the ring electrode position, and the ring electrode installation must be optimized. However, the ring electrode location must affect the nozzle and substrate to ensure that the spray pattern differs from that of the existing system. Thus, electro spray patterns in spray systems acting under various experimental conditions must be investigated.<sup>46</sup>

In comparison with the existing system, the ring electrode system may particularly overcome the low flow rate of electro spraying by increasing the water concentration. This change may render the ring electrode system applicable to the film-coating process. Most of the previous studies that involved fixed ring locations have been restricted to comparative experiments concerning the presence or absence of ring electrodes.

In this study, we compared and analyzed ring electrode locations and droplet characteristics based on the ring position and the electro spray pattern and droplet size characteristics based on the presence or absence of a ring electrode.

## 2. METHODS

**2.1. Materials.** Ethyl alcohol (94%, Ducksan), which is an organic and polar solvent commonly used in mixed solutions, was used to determine the spraying mode and droplet characteristics based on ring electrode parameters. It has a lower surface tension and electrical conductivity than pure water; hence, a stable cone-jet mode is obtained at a low applied voltage. Table 1 presents information about ethyl alcohol consumption.

Table 1. Solution Agitation Data

solution	density (kg/m <sup>3</sup> )	conductivity (μs/cm)	viscosity (mPa·s)	surface tension (mN/m)
ethyl alcohol	789	0.219	1.1	22.32

**2.2. Experimental Setup.** Figure 1 depicts the electro spraying setup used in this study. The fluid and voltage supplies and the measuring and control units constitute the experimental device diagram. The NE-1000-model syringe pump with a volume of 1 cc (HSW Norm-Ject) and a radial metal nozzle (single metal nozzle, NNC-MN 17GA, ID:1.0 mm) was used for the fluid supply unit. For the ring, aluminum was treated and directly utilized. Moreover, a ring holder was produced to change the height and apply the respective voltage. The substrate was produced in a cylindrical shape using aluminum (D, 45 mm; H, 10 mm). The top surface was flattened using a milling machine.<sup>41</sup> The cover was made of acrylic and had a ring and double cover to minimize changes in the internal environment. The board height was modified by attaching a support jack. The ring height was adjusted by placing a support within the cover.<sup>41</sup>

A variable high-voltage power supply (Korea Switching, B150; 30 kV, 15 mA) was used as the voltage supply of the nozzle and the ring. The cathode was connected to the nozzle and ring, whereas the anode was connected to the substrate. The power supply minimized hysteresis by varying the voltage using an internal controller. A high-speed camera (Phantom

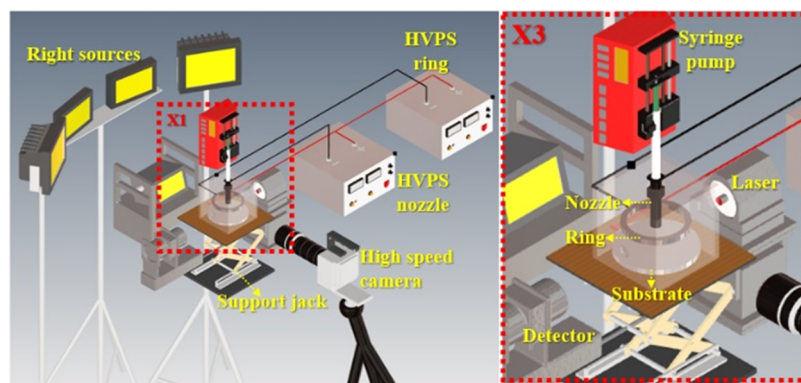


Figure 1. Experimental setup of the electro spraying technique (with a ring electrode).

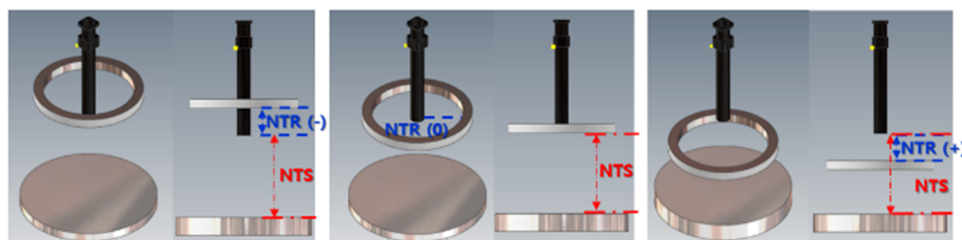


Figure 2. Nozzle-to-ring location.

VEO E310L, maximum resolution:  $512 \times 512$ , sample rate: 11,500 fps) was used for spray images. Spray flow images were obtained using an appropriate source (i.e., a halogen lamp and light-emitting diode (LED)). In all experimental conditions, more than 250 images were used. Visualization was conducted once the spray pattern achieved a steady state.<sup>47</sup>

For lighting, three rear LED lights and two front halogen lights were used to obtain the images. Discerning the subject when shooting an object in the backlight was generally easy. The spray pattern contour can be highlighted using the front oblique light, resulting in an outstanding shape. Five lights were used to assess the spray pattern.<sup>47</sup>

The high-speed camera was set to  $\geq 150$  value frames. Its shutter speed was set to  $1/11,000$  s because the light frequency was 60 Hz. The aperture setting value was tightened to F9 to guarantee the field depth. Malvern MLXA-A12-635-5, which exploits the laser diffraction principle, was used to determine the Sauter mean diameter (SMD) and the distribution of droplets sprayed from the nozzle.<sup>48</sup>

**2.3. Experimental Conditions.** Figure 2 shows a schematic representation of the distance between the nozzle and the ring, expressed as the nozzle-to-ring (NTR) distance, whereas that between the nozzle and the substrate is expressed as the nozzle-to-substrate (NTS) distance. The ring was installed to assess the electric field effect, depending on its position. For the NTR distance, NTR (−) and (0) represent the NTR distance based on the bottom of the ring, whereas NTR (+) represents the NTR distance based on the top of the ring. The ring was made of aluminum to minimize the electrical resistance.

Table 2 presents the experimental conditions. The ring diameter (RD) was set to 15, 20, 30, and 40 mm. The NTR distances were set to −20, −10, 0, 5, 10, and 20 mm. The experiment was performed by using a flow rate of 1.5 mL/h. The applied ring voltage (RV) was gradually increased from 0 to 7 kV to check the hysteresis. The experiments were

Table 2. Experimental Conditions for the Ring Electrode

condition	value
ring diameter (mm)	15, 20, 30, and 40
nozzle-to-ring distance (NTR, mm)	−20, −10, 0, 5, 10, and 20
ring voltage (kV)	0–7
ambient temperature (°C)	25
relative humidity (%)	$40 \pm 10$

conducted at the nozzle-applied voltage, at which a stable cone-jet mode is formed. Double covers were fitted to reduce the influence of the external environment and eliminate the physical changes. In addition, the temperature and relative humidity were monitored. The experiments were performed at an ambient temperature of 25 °C and a relative humidity of  $40 \pm 10\%$ .<sup>41</sup>

### 3. RESULTS AND DISCUSSION

**3.1. Spray Image of the Experiment.** Figure 3 shows the spray image obtained at a flow rate of 1.5 mL/h, an NTS distance of 45 mm, an NTR (+) of 10 mm, and an RV of 0 kV. The cone length reduced as the applied voltage increased,

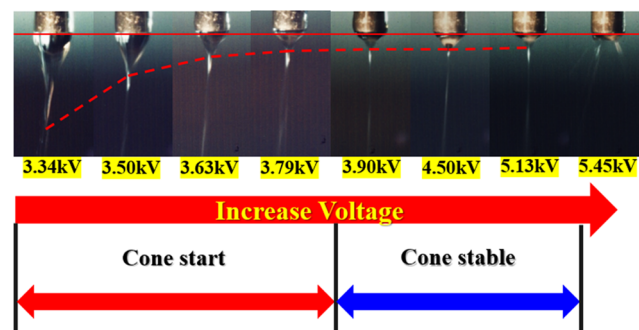
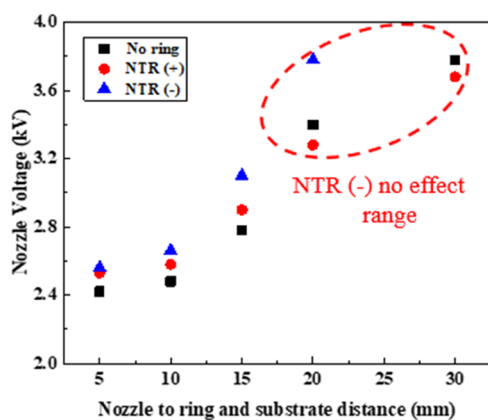


Figure 3. Spray image of the cone jet based on voltage.

indicating a stable spraying mode. Several cones were generated when the applied voltage increased to 5.45 kV or higher. A further increase in the applied voltage resulted in the disappearance of the cones and the formation of multiple lines of jets. The cone range was divided into cone start, stable cone, and cone end subranges. A cone was generated in the cone start portion, but it was unstable and did not display a continuous spray pattern compared with the stable cone range while spraying. In certain cases, the cone does not develop as a jet but instead instantly separates. A theoretical semiangle of  $49.3^\circ$  claimed by Taylor<sup>28</sup> was confirmed by the cone-stable range. Similar to the study of Panahi,<sup>49</sup> the thickness of the cone and the jet gradually decreased to form a stable spray pattern when the voltage applied to the nozzle increased.

### 3.2. Applied Voltage According to Ring Parameters.

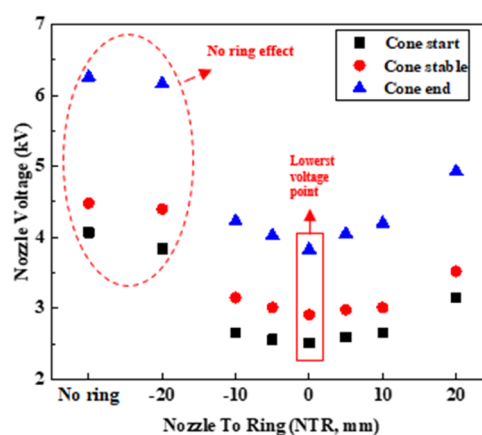
Figure 4 demonstrates a graph of the distance and voltage used



**Figure 4.** Relation of the applied voltage with the nozzle-to-ring (NTR) and nozzle-to-substrate (NTS) distances.

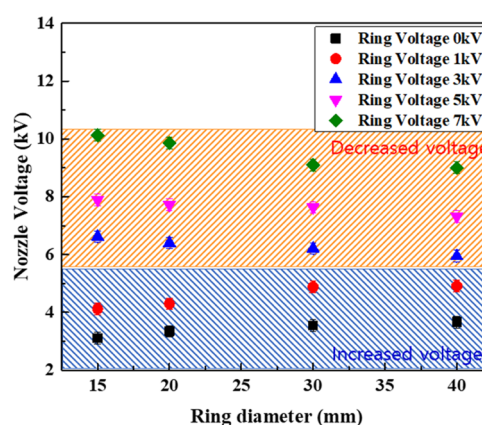
to determine the ground role of the board. The NTS distance in the absence of a ring is expressed in millimeters. The NTR distance is also expressed in millimeters in the case of NTR (+) and NTR (-). For NTR (+) and (-), experiments were conducted at a flow rate of 1.5 mL/h, an RD of 20 mm, and an NTS distance of 45 mm. The applied cone voltage increased as the distance between the substrate and the ring increased. In the case of NTR (+), the applied voltage increased similar to the case when no ring was used. For NTR (-), a difference was noted from 20 mm, caused by the insignificant effect of the electric field at NTR (-) 20 mm (or more) owing to the length of the single metal nozzle (20 mm). The ring electrode functioned as a substrate because comparable patterns were observed in all three circumstances. The difference between the cases with and without the ring was caused by structural geometry and differences in the materials and systems between the substrate and the ring.

Figure 5 presents the cone range data versus the NTR distance. The experiments were conducted at a flow rate of 1.5 mL/h, an NTS distance of 45 mm, an RD of 20 mm, and an RV of 0 kV. For NTR (0), the applied voltage increased as the distance between the NTR distance increased. This was similar to the result for the ring shown in Figure 4, which acted as a ground. The applied voltages for the NTR (-) of 20 mm and the no-ring case were similar in terms of the starting point and range because the single metal nozzle length was 20 mm and the strength of the electric field acting on the needle was weak.



**Figure 5.** Range of the applied nozzle voltage according to the NTR distance.

Figure 6 shows the graph of RD as a function of RV and cone-jet mode voltage. The experiments were conducted at a



**Figure 6.** Range of the applied nozzle voltage against ring diameter.

flow rate of 1.5 mL/h, an NTS distance of 45 mm, an NTR distance of 10 mm, and a voltage range of 0–7 kV. The applied voltage of the nozzle was increased under the condition that a stable and continuous cone-jet mode was formed. The applied nozzle voltage for the cone-jet mode formation increased with the RD below 3 kV, and the applied voltage decreased with the increase in the RD above 3 kV. This is because the ring acts as a resistance to the applied nozzle voltage when forming the cone-jet mode, and the smaller the RD, the shorter the distance, resulting in a relatively stronger electric field. Thus, for conditions above 3 kV, a smaller RD results in a higher voltage being applied to the nozzle. In addition, we found that RD differences were insignificant for RDs larger than 30 mm. This confirms the lack of an effect of the electric field on the formation of conjugate modes for RDs larger than 30 mm.

Figure 7 depicts the correlation between the ring and nozzle voltages as the NTR distance changed. The experiments were performed at a flow rate of 1.5 mL/h, an RD of 20 mm, and an NTS of 45 mm. The applied voltage of the nozzle was increased under the condition that a stable and continuous cone-jet mode was formed. The nozzle voltage for the cone started to increase as the RV increased. The electric field intensity was minimized at NTR (-) 20 mm. At  $\leq 2$  kV, which was a low RV range, the electric field effect in the ring was insignificant, and a trend similar to 0 kV was confirmed. As the

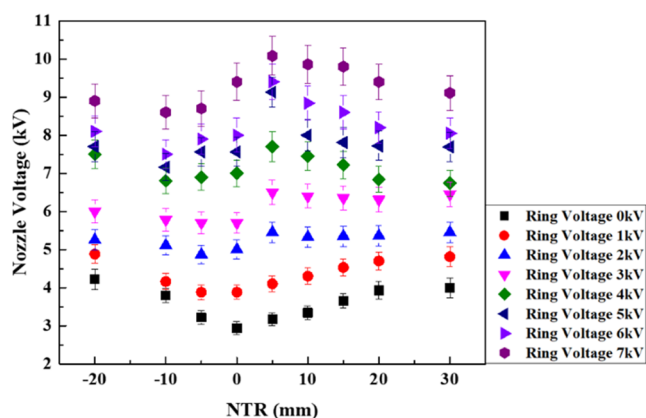


**Figure 7.** Range of the applied nozzle voltage according to the NTR distance and RV.

NTR distance increases, the applied nozzle voltage that must be applied to form the cone-jet mode increases. In the region where the electric field of the ring is rather strong ( $>4$  kV), the closer the ring is to the nozzle, the higher the applied voltage that must be applied to the nozzle to form a cone jet. In addition, the difference in applied voltage according to the NTR distance is relatively small at 3–5 kV, where the reversal phenomenon occurs.

**3.3. SMD and Its Standard Deviation.** Figure 8 demonstrates the SMD and SMD standard deviation versus

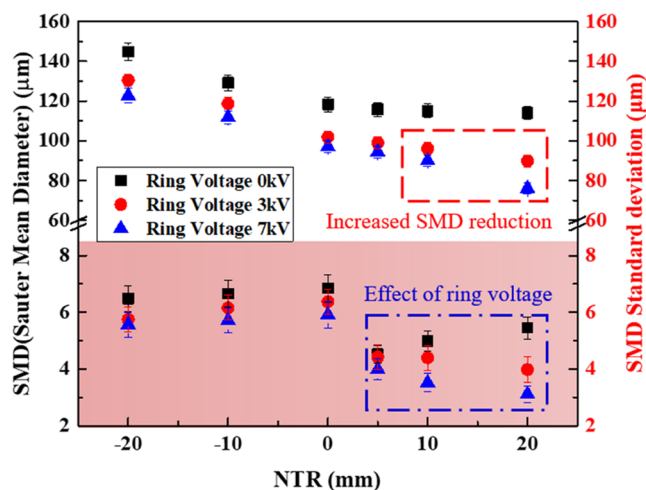


**Figure 8.** Sauter mean diameter (SMD) and its standard deviation plotted against the NTR distance.

the NTR distance. The experiments were performed at a flow rate of 1.5 mL/h, an RD of 20 mm, an NTS of 45 mm, and RVs of 0, 3, and 7 kV. The applied voltage of the nozzle was increased under the condition that a stable and continuous cone-jet mode was formed. The  $y$ -axis on the left is the SMD, and the  $y$ -axis on the right is the SMD standard deviation. To make it easier to distinguish, the SMD standard deviation has been contrasted. Similar to the earlier work of Gan,<sup>45</sup> compared to the case without a ring, the droplet size was smaller when a ring was present. The SMD also decreased as the NTR distance increased. When sprayed by the ring electrode for NTR (−), some droplets traveling in the ring direction did not form jets at the cone. They were instead promptly separated. When the NTR was (+), a repulsive force

was generated by the electric force acting on the ring during spraying, which accelerated the droplets toward the bottom of the spray, thereby forming a smaller droplet size. We found that the droplet size decreases as the NTR distance increases from − to (+). For the SMD standard deviation, we found that the SMD standard deviation increases as the NTR decreases from NTR (−) to NTR 0. As the NTR increases from NTR (0) to NTR (+), the standard deviation of the SMD decreases when the applied voltage is high and increases when the applied voltage is low. In NTR (−) conditions, liquid droplets were not produced as a jet in the cone, resulting in direct splitting in the cone. For NTR (−), some droplets stick to the ring, and as the distance from the substrate increases, the electric field acting at the bottom of the spray weakens, resulting in a wider distribution of droplets. The standard deviation of NTR (+) was reduced, similar to that in the study of Jiang,<sup>38</sup> which was caused by the electric field effect of the charged ring. The standard deviation also decreased with the increasing applied voltage when the NTR increased to (+). In the NTR (+) region, when the applied voltage of the ring is low ( $<3$  kV), the SMD standard deviation increases because a relatively small electric field acts in the direction of the bottom of the spray as the distance from the nozzle increases, and when the applied voltage is higher than 3 kV, the standard deviation of the SMD decreases as the NTR distance increases because a strong electric field is formed in the direction of the bottom of the spray between the nozzle and the ring.

Figure 9 depicts a graphical representation of the SMD and its standard deviation concerning the NTR distance and RV

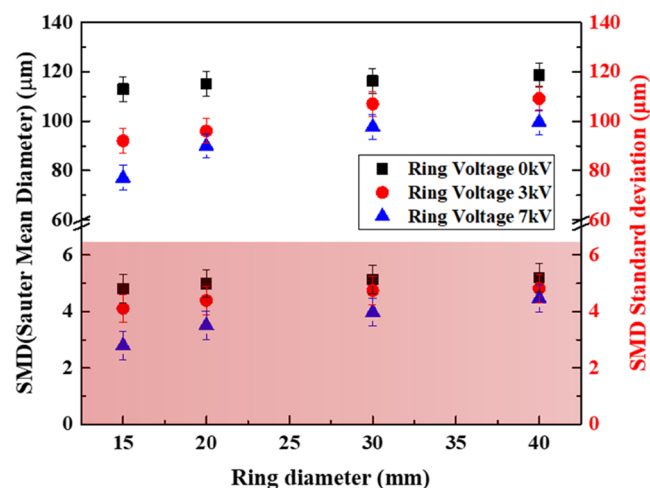


**Figure 9.** SMD and its standard deviation vs ring diameter.

variations. The  $y$ -axis on the left is the SMD, and the  $y$ -axis on the right is the SMD standard deviation. To make it easier to distinguish, the SMD standard deviation has been contrasted. The experiments were conducted at a flow rate of 1.5 mL/h, an NTS of 45 mm, and an NTR (+) of 20 mm. The applied voltage of the nozzle was increased under the condition that a stable and continuous cone-jet mode was formed. The average droplet size increased when the RD increased. For RVs of 0 kV and RDs of 30 mm or more, the SMD variation was found to be insignificant. At 0 kV and an RD of 30 mm or above, the electric field effect of the ring was insignificant. For an RV of 0 kV, a small amount of voltage was applied to the ring by the applied nozzle voltage, but no effect was found on the electric field formation. In addition, for RDs over 30 mm, similar to

that shown in Figure 6, the electric field was weakly formed owing to the large distance but did not influence the droplet size. In addition, the SMD standard deviation showed a trend similar to that of the SMD; the smaller the RD, the lower the standard deviation of the SMD. The standard deviation decreased as the applied voltage increased. The smaller the RD, the lower the standard deviation of the SMD. The standard deviation decreased as the applied voltage increased. When the applied voltage of the ring is strongly formed, the atomization acceleration increases. It is believed that the droplet size is small and is uniformly formed because polymerization is not prevented by the repulsive force of charged ions on the surface of the fluid. In addition, when the applied voltage of the ring is high, the relatively strong electric field generated accelerates the droplets to the bottom of the atomization, resulting in a smaller and more uniform droplet size.

Figure 10 depicts the SMD standard deviation of the applied voltage concerning the NTR position at a flow rate of 1.5 mL/

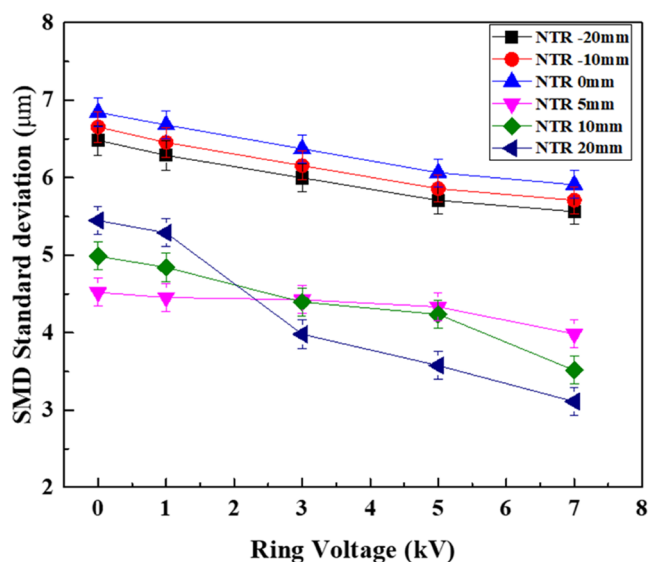


Figure 10. Standard deviation of the SMD against RV.

h, an RD of 20 mm, and an NTS distance of 45 mm. The applied voltage of the nozzle was increased under the condition that a stable and continuous cone-jet mode was formed. This shows the overall data of the effect of RV in Figure 8, which is a graph to check the change in the SMD standard deviation of the RV condition at the NTR position. Similar to that in Figure 8, the standard deviation of the SMD decreased as the applied voltage increased. In the case of NTR (+) = 20 mm, droplet polymerization and bonding did not occur owing to the installed ring at the bottom of the spray. This resulted in the smallest SMD standard deviation. Splitting was accelerated in the spray bottom direction. By contrast, at an NTR distance of 0 mm and (−) 20 mm, the standard deviation of the SMD was relatively larger because the electric field was formed upward owing to the installation on the top. For NTR (+), the standard deviation of the SMD decreased as the applied voltage increased for large NTR values. The smallest SMD standard deviation was formed at an NTR distance of 20 mm and an RV of 3 kV and above. This means that when the applied voltage of the ring increases, the applied voltage of the nozzle also increases, and the relatively strong electric field

formed in the nozzle accelerates the atomization rapidly and produces uniform and fine droplets, and the ring at the bottom of the nozzle also accelerates in the downward direction of the atomization owing to a strong electric field, resulting in the smallest SMD standard deviation. The larger the NTR (+), the smaller the SMD standard deviation according to the applied voltage of the ring.

Figure 11 shows the droplet size and the frequency data for NTR (−) 20 mm, 0 mm, and (+) 20 mm. The experiments

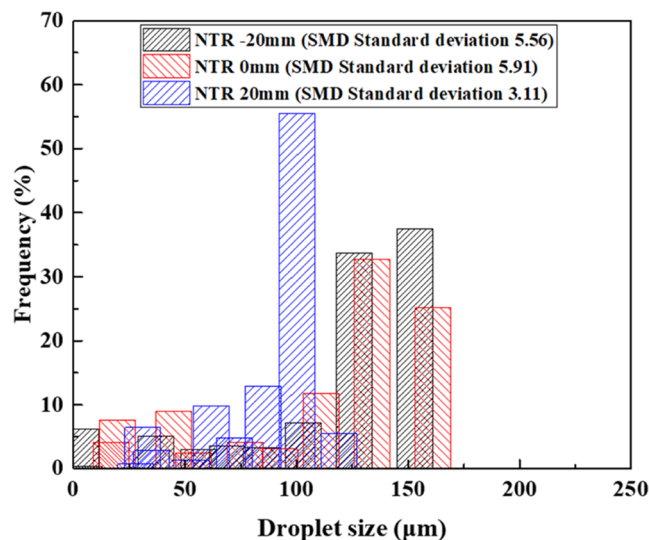


Figure 11. Droplet size and distribution according to the NTR distance.

were conducted at a flow rate of 1.5 mL/h, an NTS distance of 45 mm, and an RV of 7 kV. The applied voltage of the nozzle was increased under the condition that a stable and continuous cone-jet mode was formed. An NTR of (+) 20 mm showed the smallest SMD standard deviation. The NTR 0 mm showed the largest SMD standard deviation. NTR (20 mm) had an average droplet size of approximately 35% at 129 μm. In the NTR (+) 20 mm, the average droplet size was about 35% at 129 μm. We also found that droplets formed from 15.8 to 107.1 μm, with the highest frequency at 88.9 μm at 55.5%. This means that NTR (+) 20 mm had the narrowest droplet size range and the highest frequency of droplets formed compared with the other NTR conditions. The generation of fine droplets was smaller than that of other NTRs owing to the ring location at the bottom of atomization. This was attributed to the effect of the droplet acceleration by the ring located at the bottom of the atomization and the lack of droplet polymerization by the ions on the droplet surface after atomization from the nozzle owing to the electric field acting on the ring.

Figure 12 shows the droplet size and frequency data at applied voltages of 0, 3, and 7 kV. The experimental condition was conducted at NTR (+) 20 mm because of the smaller standard deviations. The closer the distance between the ring and the nozzle, the greater the effect on the electric field. The range of droplet size varies depending on the applied voltage, with a minimum of 13.0 and a maximum of 230.7 μm formed at an RV of 0 kV and a minimum of 15.8 and a maximum of 107.1 μm formed at an RV of 7 kV. It was confirmed that a relatively narrow droplet size range was formed with the increase in the applied voltage, and the frequency of droplets of the same size also increased with the increase in the applied

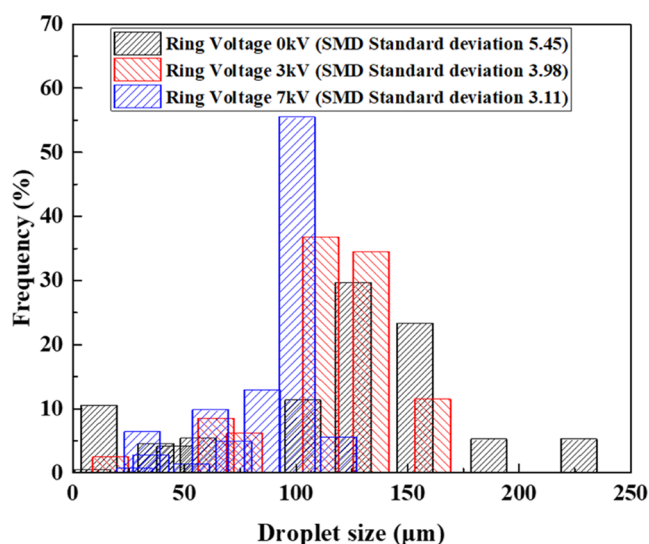


Figure 12. Variations in droplet size and distribution according to RV.

voltage. When the applied voltage increased, the strength of the electric field acting in the substrate direction, acceleration at the bottom of the atomization, and strength of the electric field in the ring all increased; hence, the droplet polymerization was significantly lower than those obtained at lower applied voltages.

Table 3 shows the SMD, its standard deviation, and relative standard deviation (RSD) data according to the experimental conditions. The RSD data can be used to identify the relationships among droplets, standard deviation, and reliability. Moreover, they are used in the field of biodiesel combustion and mass spectrometry. According to Jiang<sup>37</sup> and Ren,<sup>50</sup> it is used in the range of RSD < 15%. In this range, droplets form a monodisperse distribution with uniform formation. We found that the lower the RV, the larger the SMD and its standard deviation, whereas the higher the RV, the smaller the RSD. In contrast, the larger the RD, the larger the SMD and its standard deviation, and the larger the RSD. In the case of the NTR distance, unlike the previous two conditions, the SMD and its standard deviation were similar to the previous two conditions, but the RSD was the smallest at 10 mm. In this experiment, the conditions with the smallest SMD, standard deviation of the SMD, and RSD are an RD of 15 mm, an RV of 7 kV, and an NTR (+) of 20 mm. When installing the ring electrode, it was found that the smaller the RD, the greater the NTR (+) and the greater the distance, and the greater the applied voltage of the ring, the finer and more uniform the droplets produced.

Table 3. SMD, SMD Standard Deviation, and Relative Standard Deviation (RSD) Based on Experimental Conditions

	ring voltage (RV) (NTR 20, RD 20)	ring diameter (RD) (NTR 20, RV 7)	nozzle-to-ring (NTR) distance (RD 20, RV 7)
SMD ( $\mu\text{m}$ )	76.0–114.0	60.0–97.5	76–122.7
standard deviation ( $\mu\text{m}$ )	3.1–5.4	1.9–4.2	3.1–5.9
RSD (%)	4.1–5.3	3.1–4.3	3.9–6.1
highest SMD condition ( $\mu\text{m}$ )	0 kV (114.0 $\mu\text{m}$ )	40 mm (97.5 $\mu\text{m}$ )	–20 mm (122.7 $\mu\text{m}$ )
lowest standard deviation condition ( $\mu\text{m}$ )	7 kV (3.1 $\mu\text{m}$ )	15 mm (1.9 $\mu\text{m}$ )	20 mm (3.1 $\mu\text{m}$ )
lowest RSD condition (%)	7 kV (4.1%)	15 mm (3.1%)	10 mm (3.9%)

RSD = SMD standard deviation ( $\mu\text{m}$ )/Sauter mean diameter (SMD,  $\mu\text{m}$ )  $\times$  100(%).

Figure 13 shows a graph of NTR variations (Table 3) as a function of the experimental conditions. The RSD increases

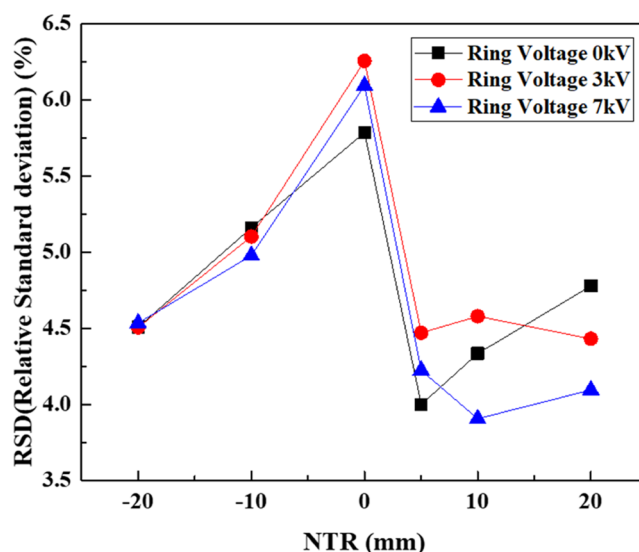


Figure 13. RSD data as a function of the NTR distance and RV.

with NTR from –20 to 0 mm and is smaller in the NTR (+) range than in the NTR (–) range. In addition, the RSD is maximum at 0 regardless of the ring applied voltage. To produce uniform droplets, an NTR distance of 0 mm must be avoided. The smallest RSD was found at an NTR (+) of 10 mm and an RV of 7 kV: it increases with NTR (+) at an RV of 0 kV and decreases at RVs of 3 kV and 5 kV. Since all experimental conditions were conducted in the stable cone-jet mode, all conditions formed RSD < 15%.

#### 4. CONCLUSIONS

1. In electrospray, it was confirmed that the electric field strength of the ring electrode is affected by the installation position and applied voltage. In particular, the inversion phenomenon appears at the ring applied voltage above 3 kV, and the smaller the NTR distance, the higher the applied voltage is required at the nozzle for cone-jet formation.
2. NTR position variation and ring diameter affect droplet size and SMD standard deviation, and we found that droplet size increases as the NTR moves from (+) to (–) and increases with increasing ring diameter. For SMD standard deviation, varies differently with respect to ring position 0, and the SMD standard deviation decreases with a smaller ring diameter.

3. Checked the RSD, which is a criterion for mono-dispersion, through the experimental parameters, and found that the conditions with the smallest RSD in this experiment were an RD of 15 mm, an RV of 7 kV, and an NTR (+) of 20 mm.

## AUTHOR INFORMATION

### Corresponding Author

Jung Goo Hong – School of Mechanical Engineering, Kyungpook National University, Daegu 41566, Republic of Korea; [orcid.org/0000-0002-1286-5728](https://orcid.org/0000-0002-1286-5728); Email: [jghong70@knu.ac.kr](mailto:jghong70@knu.ac.kr)

### Authors

Ji Yeop Kim – School of Mechanical Engineering, Kyungpook National University, Daegu 41566, Republic of Korea  
Sang Ji Lee – School of Mechanical Engineering, Kyungpook National University, Daegu 41566, Republic of Korea  
Mun Hee Lee – School of Mechanical Engineering, Kyungpook National University, Daegu 41566, Republic of Korea

Complete contact information is available at:

<https://pubs.acs.org/10.1021/acsomega.3c07402>

### Author Contributions

Conceptualization, methodology, validation, and data curation, J.Y.K., S.J.L., and M.H.L.; writing—original draft preparation, J.Y.K.; writing—review and editing, J.Y.K. and J.G.H.; and supervision, J.G.H.; All authors have read and agreed to the published version of the manuscript.

### Notes

The authors declare no competing financial interest.

## ACKNOWLEDGMENTS

This work was supported by the Human Resources Program in Energy Technology of the Korea Institute of Energy Technology Evaluation and Planning (KETEP) and was granted financial resources from the Ministry of Trade, Industry and Energy, Republic of Korea (No. 20204010600060).

## REFERENCES

- (1) Aguilera, J. M.; Chiralt, A.; Fito, A. Food dehydration and product structure. *Trends Food Sci. Technol.* **2003**, *14* (10), 432–437.
- (2) *Handbook of Industrial Drying*, 3rd ed.; Mujumdar, A. S., Ed.; CRC Press, 2006.
- (3) Berk, Z. *Food Process Engineering and Technology*; Academic Press, 2009.
- (4) Lewicki, P. P. Design of hot air drying for better foods. *Trends Food Sci. Technol.* **2006**, *17* (4), 153–163.
- (5) Vega-Mercado, H.; Góngora-Nieto, M. M.; Barbosa-Cánovas, G. V. Advances in dehydration of foods. *J. Food Eng.* **2001**, *49* (4), 271–289.
- (6) Sagar, V. R.; Kumar, P. S. Recent advances in drying and dehydration of fruits and vegetables: a review. *Int. J. Food Eng.* **2010**, *47* (1), 15–26.
- (7) Patel, R. P.; Patel, M. P.; Suthar, A. M. Spray drying technology: an overview. *Indian J. Sci. Technol.* **2009**, *2* (10), 44–47.
- (8) Paul, A.; Astatkie, E.; Martynenko, A. Electrohydrodynamic drying of fruit slices: Effect on drying kinetics, energy consumption, and product quality. *J. Food Process. Preserv.* **2022**, *46* (10), No. e16812, DOI: [10.1111/jfpp.16812](https://doi.org/10.1111/jfpp.16812).
- (9) Sosnik, A.; Seremeta, K. P. Advantages and challenges of the spray-drying technology for the production of pure drug particles and drug-loaded polymeric carriers. *Adv. Colloid Interface Sci.* **2015**, *223*, 40–54.
- (10) Burgain, J.; Gaiani, C.; Linder, M.; Scher, J. Encapsulation of probiotic living cells: From laboratory scale to industrial applications. *J. Food Eng.* **2011**, *104* (4), 467–483.
- (11) Cai, Y. Z.; Corke, H. Production and Properties of Spray-dried *Amaranthus* Betacyanin Pigments. *J. Food Sci.* **2000**, *65* (7), 1248–1252.
- (12) Bdour, A.; Khuloud Electrohydrodynamic drying of viscous materials and agar gel. Ph.D. Thesis; McGill University: Quebec, Canada, 2000.
- (13) Cal, K.; Sollohub, K. Spray Drying Technique. I: Hardware and Process Parameters. *J. Pharm. Sci.* **2010**, *99* (2), 575–586.
- (14) Sanders, J. E.; Wang, L.; Brinkley, G.; Gardner, D. J. Production of nano-scale cellulose nanocrystal powder via electrospray drying (ESD) for sustainable composites. *Cellulose* **2023**, *30*, 6303–6315.
- (15) Silva, P. M.; Prieto, C.; Lagaron, J. M.; Pastrana, L. M.; Coimbra, M. A.; Vicente, A. A.; Cerqueira, M. A. Food-grade hydroxypropyl methylcellulose-based formulations for electrohydrodynamic processing: Part I – Role of solution parameters on fiber and particle production. *Food Hydrocolloids* **2021**, *118*, No. 106761.
- (16) Anukiruthika, T.; Moses, J. A.; Anandharamkrishnan, C. Electrohydrodynamic drying of foods: Principle, applications, and prospects. *J. Food Eng.* **2021**, *295*, No. 110449.
- (17) Davoodi, P.; Feng, F.; Xu, Q.; Yan, W. C.; Tong, Y. W.; Srinivasan, M. P.; Sharma, V. K.; Wang, C. H. Coaxial electrohydrodynamic atomization: Microparticles for drug delivery applications. *J. Controlled Release* **2015**, *205*, 70–82.
- (18) Mendes, A. C.; Chronakis, I. S. Electrohydrodynamic encapsulation of probiotics: A review. *Food Hydrocolloids* **2021**, *117*, No. 106688.
- (19) Gomez, A.; Bingham, D.; Juan, L. D.; Tang, K. Production of protein nanoparticles by electrospray drying. *J. Aerosol Sci.* **1998**, *29* (5–6), 561–574.
- (20) Niamah, A. K.; Al-Sahly, S. T. G.; Ibrahim, S. A.; Verma, D. K.; Thakur, M.; Singh, S.; Patel, A. R.; Aguilar, C. N.; Utama, G. L. Electro-hydrodynamic processing for encapsulation of probiotics: A review on recent trends, technological development, challenges, and future prospect. *Food Biosci.* **2021**, *44*, No. 101458.
- (21) Tanhaei, A.; Mohammadi, M.; Hamishehkar, H.; Hamblin, M. R. Electro-spraying as a novel method of particle engineering for drug delivery vehicles. *J. Controlled Release* **2021**, *330*, 851–865.
- (22) Zafar, H. S.; Asefi, N.; Siahpoush, V.; Roufegarinejad, L.; Alizadeh, A. Preparation of egg white powder using electrohydrodynamic drying method and its effect on quality characteristics and functional properties. *Food Chem.* **2023**, *426*, No. 136567.
- (23) Sverdlov Arzi, R.; Sosnik, A. Electrohydrodynamic atomization and spray-drying for the production of pure drug nanocrystals and co-crystals. *Adv. Drug Delivery Rev.* **2018**, *131*, 79–100.
- (24) Jayaprakash, P.; Gaiani, C.; Edoth, J. M.; Borges, F.; Beaupeux, E.; Maudhuit, A.; Desobry, S. Comparison of Electrostatic Spray Drying, Spray Drying, and Freeze Drying for Lacticaseibacillus rhamnosus GG Dehydration. *Foods* **2023**, *12* (16), No. 3117.
- (25) Tapia-Hernandez, J. A.; Torres-Chavez, P.; Ramirez-Wong, B.; Rascon-Chu, A.; Plascencia-Jatomea, M.; Barreras-Urbina, C. G.; Rangel-Vazquez, N. A. Rodriguez-Felix, Micro- and Nanoparticles by Electro-spray: Advances and Applications in Foods. *J. Agric. Food Chem.* **2015**, *63* (19), 4699–4707.
- (26) Ni, J. B.; Bi, Y. X.; Vidyarthi, S. K.; Xiao, H. W.; Han, L. D.; Wang, J.; Fang, X. M. Non-thermal electrohydrodynamic (EHD) drying improved the volatile organic compounds of lotus bee pollen via HS-GC-IMS and HS-SPME-GC-MS. *LWT* **2023**, *176*, No. 114480.
- (27) Chen, X.; Jia, L.; Yin, X.; Cheng, J.; Lu, J. Spraying modes in coaxial jet electrospray with outer driving liquid. *J. Phys. Fluids* **2005**, *17*, No. 032101.
- (28) Taylor, G. I. Disintegration of Water Drops in an Electric field. *Proc. R. Soc. London, Ser. A* **1964**, *280* (1382), 383–397.

- (29) Kim, J. Y.; Lee, S. J.; Baik, G. Y.; Hong, J. G. Effects of Working Fluids on Spray Modes and Atomization Characteristics in Electro-spray. *J. Korean Soc. Precis. Eng.* **2021**, *38* (1), 61–68.
- (30) Rahmanpour, M.; Ebrahimi, R. Numerical Simulation of Highly Charged Droplets Dynamics with Primary Break-up in Electro-spray at Sub Rayleigh Limit. *J. Appl. Fluid Mech.* **2017**, *10* (2), 541–550.
- (31) Wu, Y.; Mackay, J. A.; McDaniel, J. R.; Chilkoti, A.; Clark, R. L. Fabrication of Elastin-Like Polypeptide Nanoparticles for Drug Delivery by Electro-spraying. *Biomacromolecules* **2009**, *10* (1), 19–24.
- (32) Yuill, E. M.; Sa, N.; Ray, S. J.; Hieftje, G. M.; Baker, L. A. Electro-spray Ionization from Nanopipette Emitters with Tip Diameters of Less than 100 nm. *Anal. Chem.* **2013**, *85* (18), 8498–8502.
- (33) Määttä, K. R.; Eldin, A. K.; Torronen, A. R. High-Performance Liquid Chromatography (HPLC) Analysis of Phenolic Compounds in Berries with Diode Array and Electro-spray Ionization Mass Spectrometric (MS) Detection: Ribes Species. *J. Agric. Food Chem.* **2003**, *51*, 6736–6744.
- (34) Wu, X.; Prior, R. L. Identification and Characterization of Anthocyanins by High-Performance Liquid Chromatography–Electro-spray Ionization–Tandem Mass Spectrometry in Common Foods in the United States: Vegetables, Nuts, and Grains. *J. Agric. Food Chem.* **2005**, *53*, 3101–3113.
- (35) Takats, Z.; Wiseman, J. M.; Gologan, B.; Cooks, R. G. Mass Spectrometry Sampling Under Ambient Conditions with Desorption Electro-spray Ionization. *Science* **2004**, *306* (5695), 471–473.
- (36) Gao, D.; Zhou, J. G. Designs and applications of electro-hydrodynamic 3D printing. *Int. J. Bioprint.* **2019**, *5* (1), No. 172.
- (37) Jiang, Z.; Gan, Y.; Ju, Y.; Liang, J.; Zhou, Y. Experimental study on the electro-spray and combustion characteristics of biodiesel-ethanol blends in a meso-scale combustor. *Energy* **2019**, *179*, 843–849.
- (38) Kuwahata, Y.; Takehara, H.; Ichiki, T. Comprehensive study on electro-spray deposition in the single Taylor cone–jet mode by changing the spatial electric potential using a ring-shaped ternary electrode. *AIP Adv.* **2020**, *10* (4), No. 045107.
- (39) Ali, A.; Lee, Y. W.; Choi, K. H.; Jo, J. D. Effect of Poly(4-vinylphenol) Concentration Increase on Deposition Rate of Dielectric Thin Film Fabrication by Using Electrohydrodynamic Atomization. *J. Electron. Mater.* **2013**, *42*, 3512–3518.
- (40) Liao, Y.; Fukuda, T.; Kamata, N. Improved Morphology of Poly(3,4-ethylenedioxythiophene):Poly(styrenesulfonate) Thin Films for All-Electro-spray-Coated Organic Photovoltaic Cells. *Adv. Mater. Sci. Eng.* **2016**, *2016*, No. 9734854.
- (41) Kim, J. Y.; Lee, S. J.; Hong, J. G. Spray Mode and Monodisperse Droplet Properties of an Electro-spray. *ACS Omega* **2022**, *7* (32), 28667–28674.
- (42) Tang, L.; Kebarle, P. Effect of the conductivity of the electro-sprayed solution on the electro-spray current. Factors determining analyte sensitivity in electro-spray mass spectrometry. *Anal. Chem.* **1991**, *63* (23), 2709–2715.
- (43) Tang, K. The Electro-spray: Fundamentals and feasibility of its application to targeted drug delivery by inhalation. Ph.D. Thesis; Yale University: New Haven, U.S., 1994.
- (44) Le, N. T.; Myrick, J. M.; Seigle, T.; Huynh, P. T.; Krishnan, S. Mapping electro-spray modes and droplet size distributions for chitosan solutions in unentangled and entangled concentration regimes. *Adv. Powder Technol.* **2018**, *29* (12), 3007–3021.
- (45) Gan, Y.; Jiang, Z.; Li, H.; Luo, T.; Chen, X.; Shi, Y.; Yan, Y.; Yan, Y. A comparative study on droplet characteristics and specific charge of ethanol in two small-scale electro-spray systems. *Sci. Rep.* **2019**, *9*, No. 18791.
- (46) Shen, H.; Jia, H.; Kang, Y. Electrical Characteristics and Electrohydrodynamic Flows in Electrostatic Precipitator of Six Shaped Discharge Electrodes. *J. Appl. Fluid Mech.* **2020**, *13* (6), 1707–1718.
- (47) Kim, J. Y.; Lee, S. J.; Baik, G. Y.; Hong, J. G. Viscosity Effect on the Electro-spray Characteristics of Droplet Size and Distribution. *ACS Omega* **2021**, *6* (44), 29724–29734.
- (48) Ku, K. W.; Hong, J. G.; Park, C. W. EFFECT OF ASSIST-AIR OF TWIN FLUID ATOMIZER ON UREA THERMAL DECOMPOSITION. *Atomization Sprays* **2015**, *25* (10), 895–915.
- (49) Panahi, A.; Pishavar, A. R.; Tavakoli, M. R. Numerical simulation of jet mode in electro-spraying of Newtonian and viscoelastic fluids. *Int. J. Multiphase Flow* **2020**, *129*, No. 103302.
- (50) Ren, J.; Ma, Y.; Ma, M.; Ding, J.; Jiang, J.; Zheng, X.; Han, X. Rapid ultra-performance liquid chromatography-tandem mass spectrometry method for the simultaneous determination of three characteristic urinary saccharide metabolites in patients with glycogen storage diseases (type Ib and II). *J. Chromatography B* **2023**, *1229*, No. 123900.